

Cite this: *Nanoscale*, 2012, **4**, 1760

www.rsc.org/nanoscale

PAPER

Tin oxide nanowire sensor with integrated temperature and gate control for multi-gas recognition†

Eric N. Dattoli,* Albert V. Davydov and Kurt D. Benkstein

Received 30th November 2011, Accepted 29th December 2011

DOI: 10.1039/c2nr11885h

The selectivity of a chemiresistive gas sensor comprising an array of single-crystalline tin oxide nanowires (NWs) is shown to be greatly enhanced by combined temperature and gate voltage modulation. This dual modulation was effected by a novel microsensor platform that consisted of a suspended nitride membrane embedded with independently addressable platinum heater and back-gate structures. The sensor was evaluated in a chemical vapor exposure test consisting of three volatile organic compound (VOC) analytes in an air background; VOC concentrations ranged from 20 $\mu\text{mol/mol}$ to 80 $\mu\text{mol/mol}$. During the exposure test, the temperature and gating conditions of the NW sensor were modulated in order to induce variations in the sensor's analyte response behavior. By treating these temperature- and gate-dependent analyte response variations as an identifying "fingerprint," analyte identification was achieved using a statistical pattern recognition procedure, linear discriminant analysis (LDA). Through optimization of this pattern recognition procedure, a VOC recognition rate of 98% was obtained. An analysis of the recognition results revealed that this high recognition rate could only be achieved through the combined modulation of temperature and gate bias as compared to either parameter alone. Overall, the highly accurate VOC analyte discrimination that was achieved here confirms the selectivity benefits provided by the utilized dual modulation approach and demonstrates the suitability of miniature nanowire sensors in real-world, multi-chemical detection problems.

1. Introduction

Nanowires (NWs), owing to their quasi-one-dimensional morphology and associated large surface-area-to-volume ratios, have been investigated as the transducer material in a wide range of sensors designed for either biochemical,¹ mass,² or optical³ detection. For the field of gas-sensing a certain class of these materials, semiconducting metal oxide (MOX) nanowires, has received a substantial amount of attention.^{4,5} Reports have shown that MOX nanowires can be employed as gas-phase, chemiresistive sensors with high sensitivities to target concentrations of 1 $\mu\text{mol/mol}$ and lower.^{6,7} However, pristine MOX nanowire sensors are relatively unselective due to their cross-sensitivity to a broad range of gases.⁸ This cross-sensitivity includes many volatile organic compounds (VOCs), some of

which have toxic, flammable or other hazardous characteristics. The monitoring and detection of VOC concentration levels is of prime importance in a diverse range of areas such as homeland security, workplace safety, and even medical diagnosis, where VOCs may be disease biomarkers found in exhaled breath.^{9–11} If the selectivity problem could be adequately rectified, MOX nanowire sensors would be well-suited to serve in these application areas since they possess advantages in terms of sensitivity and miniaturization capabilities as compared to conventional polycrystalline film MOX transducer materials.⁸ Consequently, the demonstration of such miniature nanowire sensors could contribute to the realization of highly-portable VOC detection systems.

So far, approaches for improving the selectivity of MOX nanowires have focused on the use of multi-element arrays of simultaneously operating NW sensors possessing either varied surface functionalizations^{12,13} or temperatures.¹⁴ Additionally, nanowire sensors have been employed as discrete elements in hybrid material chemiresistor arrays.^{15,16} Altogether, these multi-element sensor arrays have been designated by the term 'electronic nose' (e-nose) due to their functional similarity to human noses that operate using hundreds of different types of olfactory receptors working in parallel. Although the e-nose approach is presently used in commercially available MOX thin- or thick-film chemiresistive gas sensor systems, large numbers of sensors are required in order to enhance selectivity. A recent review

Material Measurement Laboratory, National Institute of Standards and Technology (NIST), 100 Bureau Drive, MS 8362, Gaithersburg, MD, 20899-8362. E-mail: edattoli@gmail.com

† Electronic supplementary information (ESI) available: Additional information pertaining to the following is available: microhotplate/sensor device structure, microhotplate thermal/electric simulation, measurements of sensor's transient response to changes in temperature and gating conditions, sensor measurement cross-correlation information, detailed analyte training/recognition results, *I-V* sweeps of sensor, details of the simulation of the electrostatic interaction between the NW and back-gate, and additional sensor response plots vs. gate bias. See DOI: 10.1039/c2nr11885h

found that present commercial MOX sensor systems typically employ from 6 to 38 hybrid MOX sensors.¹⁷ Due to their complexity, such many-element sensor arrays are impractical for realizing ultra-miniature gas sensor systems that would be well-suited to portable VOC monitoring applications.^{17,18}

As an alternative strategy to employing a large number of sensors in fixed operating configurations, the controlled modulation of the operating conditions of either one or a small number of sensors has been examined as a means to achieve selectivity.^{19,20} Operating conditions, such as temperature²¹ and electrostatic gating,²² have been shown to affect MOX NW sensing behavior *via* modulation of the chemical interactions that occur between the sensing material and target analytes. These surface interactions, the most well-known being the chemisorption and catalytic reaction of the analytes, are significantly influenced by temperature and electrostatic gating conditions as a result of two major effects. First, chemisorption and catalysis are both temperature-activated processes, and as such, are well-known to be directly affected by temperature conditions.²³ Second, the bulk electrical properties of semiconducting sensing materials, in particular their free carrier concentrations, are strongly influenced by both temperature and electrostatic gating conditions. These electrical properties have a critical bearing on sensing behavior since the chemisorption and catalytic reactions that take place on semiconductors rely on charge transfer interactions with the underlying bulk.^{24,25}

Here, we present a new approach that takes advantage of these effects by means of a novel nanowire sensor design that allows for the rapid modulation of both temperature and electrostatic gating conditions. During operation of the sensor, the controlled modulation of these operating conditions was carried out in order to induce variations in the sensor's analyte response behavior. Using these temperature- and gate-dependent analyte response variations as an identifying "fingerprint," analyte identification was achieved through the use of a statistical pattern recognition technique, linear discriminant analysis (LDA). To evaluate the extent that this dual modulation approach increased the amount of discriminatory information obtained from the sensor, the recognition accuracy of the modulated sensor was evaluated in a VOC analyte exposure test. An in-depth analysis of the statistical recognition results revealed that the modulation of both temperature and gating conditions significantly improved the VOC recognition capability of the sensor. To gain insight into the origin of this improvement, the effect of particular temperature and gate-bias operating conditions on the recognition accuracy will be explored.

For this study, simultaneous temperature and gate modulation were provided in an integrated fashion by a specially designed microsensor platform. Using a resistive heater embedded within the platform, the NW sensor was operated at an elevated temperature range in which MOX sensing interactions occur.²⁶ The microsensor platform structurally consisted of a suspended silicon nitride membrane, fabricated using standard micro-machining techniques. This suspended structure provided for a large degree of thermal isolation from the surrounding silicon substrate so as to enable low-power heater operation (32 mW maximum power consumption). Gate modulation was realized using an embedded back-gate electrode such that the NW chemiresistive sensor was operated in a field-effect transistor

(FET) configuration. Overall, the microsensor platform, commonly referred to as a microhotplate,²⁴ provided for the necessary sensor modulation capabilities while only requiring small amounts of space and power. Such characteristics are of particular benefit towards the development of new gas sensor systems with improved portability and deployability in sensor networks.

Single-crystal tin oxide nanowires, which have been previously shown to be capable sensing materials,^{21,25,27–29} were utilized. For this study these SnO₂ nanowires provided two significant benefits: (1) their single-crystalline structure yielded high carrier mobilities (>100 cm²/V·s as determined previously³⁰) that resulted in strong gate modulation effects; and (2) their large surface-area-to-volume ratio facilitated a significant amount of gate coupling to the exposed nanowire surfaces that are involved in sensing. Distinctly, these features are not provided by the polycrystalline films traditionally used in MOX sensor devices.

2. Experimental section

2.1 Tin oxide nanowire growth

SnO₂ nanowires were grown *via* a chemical vapor deposition process on a Si (100) substrate with 20 nm diameter Au catalyst nanoparticles (Ted Pella, Inc.‡) dispersed on the surface.³¹ The substrates, along with a mixture of precursor Sn powder (0.2 g) and an *in situ* dopant source, Ta powder (0.015 g), were placed in a ceramic boat that was then situated in the center of a horizontal tube furnace. Subsequently, growth was carried out at 900 °C for 0.2 h under a 300 standard mL/min flow of Ar at laboratory ambient pressure. In this growth procedure, *in situ* Ta doping of the SnO₂ nanowires was carried out so as to ensure reasonable n-type conductivity and to facilitate ohmic behavior of the electrical contacts, as has been detailed previously.³⁰ Following growth, nanowire crystal structure was verified by X-ray diffraction as tetragonal (rutile) with $a = 0.474$ nm and $c = 0.319$ nm. NWs mostly in the range of 30 nm to 80 nm in diameter and tens of micrometers in length were randomly oriented on the substrate; their growth axis was determined as [101] from electron backscatter diffraction measurements (see Figures S1, S2). Energy dispersive spectroscopy measurements of the as-synthesized nanowires confirmed their material composition and a Ta-doping level of <1% (atomic), *i.e.*, below detection limits.

2.2 Sensor device fabrication

These synthesized nanowires were utilized as the gas-sensitive material in a chemiresistive sensor that was situated on the top surface of a microhotplate platform, which provided integrated temperature and gate control. The microhotplate platform consisted of a Pt resistive heater and center-situated back-gate electrode, both of which were fully embedded within a suspended silicon nitride (SiN_x) membrane, as shown in the device

‡ Certain commercial equipment, instruments or materials are identified in this report to specify adequately the experimental procedure. Such identification does not imply recommendation or endorsement by the National Institute of Standards and Technology, nor does it imply that the materials or equipment identified are necessarily the best available for the purpose.

schematic (Fig. 1a, S3, S4). This microhotplate platform was fabricated according to the following procedure. First, 300 nm of low-stress (Si-rich) silicon nitride was deposited onto a Si substrate using low-pressure chemical vapor deposition (LPCVD) at 835 °C. On the next layer, the meander heater and back-gate electrode were patterned by lift-off using an e-beam evaporated Ta/Pt film (20 nm/200 nm thickness). This heater/gate layer was then completely embedded within nitride by carrying out a second nitride deposition using identical conditions as the first. Next, a backside KOH Si etch (30% concentration, 90 °C) was performed to achieve membrane release. The membrane possessed the areal dimensions of 360 μm \times 360 μm (see Figure S3). In order to improve the planarity of the top surface for the later deposition of additional device layers, a 160 nm thick layer of spin-on-glass (Filmtronics 700A \ddagger) was spun-on and annealed at 500 °C.

Subsequently, a discontinuous layer of roughly aligned SnO₂ nanowires was deposited on this platform using a shear force-based process termed contact printing.³² As-grown SnO₂ nanowire growth substrates were placed in contact with the top microhotplate surface and in a controlled fashion were slid in a uniform direction \approx 1 mm with a speed of \approx 0.2 mm/s while under an applied pressure of \approx 4 kPa from an above-placed weight. Lastly, metal electrodes that served as nanowire top contacts were realized by lift-off patterning of an e-beam evaporated Ti/Pt film (20 nm/200 nm). The electrodes possessed an electrode-to-electrode gap of 5 μm . Nanowires not held down by Ti/Pt electrodes were removed from the microhotplate surface *via* solvent cleaning after lift-off.

Although several devices were fabricated and found to possess similar sensing characteristics, the detailed characterization of

a single representative device, shown in Fig. 1, is the focus of this report. A total of 23 SnO₂ nanowires were found to bridge this device's sensing electrodes. The bridging nanowires possessed a mean diameter of 51 nm \pm 21 nm (Figure S5). A distribution of NW alignment angles was present in the array, resulting in several overlapped nanowires. Such a feature is likely to have some impact on sensing characteristics, but its significance was unexamined in this study.

The configuration of this sensor, which comprised multiple nanowires working in parallel, provided for two key benefits as compared to a single nanowire configuration. First, the use of multiple nanowires has the effect of averaging out wire-to-wire variations, such as diameter or contact differences, thus improving the confidence that measurements reflected the nanowires' intrinsic properties.³³ Second, the sensor base conductance level was high enough (\approx 1 μS) to allow use of readily available measurement electronics, even at low operating temperatures.

2.3 Microhotplate temperature control

After fabrication, the thermal/electrical properties of the microhotplate structure were characterized by measurement of the temperature coefficient of resistance (TCR) of the embedded Ta/Pt thin-film meander heater. A microhotplate fabricated under identical conditions was loaded into a box furnace and the resistance of its meander heater was monitored up to a furnace temperature of 150 °C. A TCR of $1.90 \times 10^{-3} \Omega/(\Omega \cdot \text{K})$ was determined from this measurement, which agreed closely with studies on similarly structured microhotplates.³⁴

During sensor operation, temperature control was achieved by application of a DC voltage to the integrated Pt heater. The temperature generated by the heater (denoted T_{heater}) was inferred from the monitored value of heater resistance using its experimentally measured temperature coefficient of resistance (TCR).³⁷ The temperature profile at the surface of the microhotplate was non-uniform, and as a result T_{heater} as inferred by this method represents an average temperature over the entire meander heater area. To gain insight into the extent of this temperature non-uniformity and to ensure that the integrated gate electrode did not substantially degrade the temperature profile, a thermal/electric finite element simulation of the entire structure under typical operating conditions ($T_{\text{heater}} \approx 300$ °C) was carried out. A surface temperature range of 321 °C to 333 °C was obtained in the sensor active area (between the sensor electrodes); see Fig. 1c. This range corresponds to a $\pm 2\%$ temperature variation that was deemed tolerable for this study.

2.4 Sensor operation and testing

Sensor characterization was carried out in a custom-built gas delivery system. The microhotplate/sensor device was mounted onto a dual in-line package and enclosed within a flow cell. VOC analytes were delivered from gas cylinders with certified concentrations, and mixed with a flowing zero-grade, dry air background. The total gas flow rate was maintained at 1 standard L/min throughout the sensing experiment using computer-controlled mass flow controllers. Analyte concentrations were varied by changing the mixing ratios of the analyte gas stream

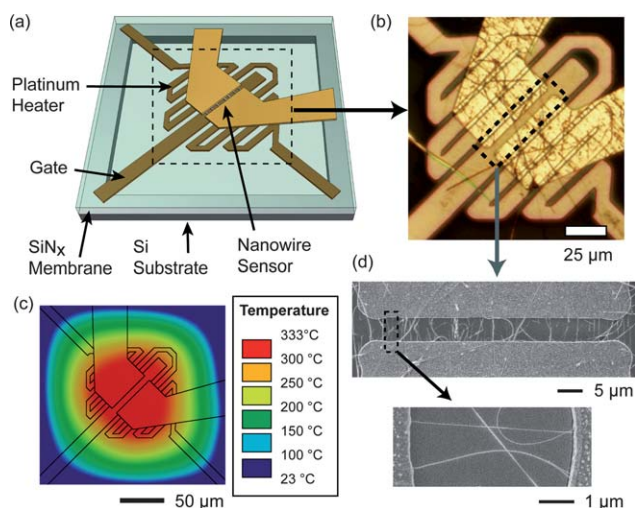


Fig. 1 Overview of Nanowire Microhotplate Sensor. (a) Schematic view of the sensor fabricated on a nitride membrane-based microhotplate platform. A Pt meander heater is embedded in the nitride membrane, while the nanowire sensor is situated on the membrane top surface in the heater center. (b) Optical image of the examined microhotplate/sensor device. (c) Electrical/thermal simulation result of the microhotplate operated under typical sensing conditions ($T_{\text{heater}} \approx 300$ °C). (d) Scanning electron microscopy (SEM) images of the nanowire sensor. Upper, a view of the entire sensor active area. Lower, a view of the indicated area (rotated clockwise 90°) that shows 2 bridging SnO₂ nanowires.

and the background air stream. The conductance of the nanowire sensor was measured by applying a constant voltage of 0.3 V to the sensing electrodes (termed V_{ds}) and monitoring the current using a Keithley 2410 SourceMeter.[‡] The acquisition time for the current measurements was 110 ms. A dual-channel programmable voltage source was used to bias the heater and gate electrode (V_{gs}), while the microhotplate resistance was monitored using a Keithley 2001[‡] multimeter. The room temperature resistance of the Pt heater was 90 Ω .

Preliminary testing of the sensor under fixed operating conditions confirmed that the SnO₂ NW sensor possessed a typical chemiresistive response upon exposure to VOC analytes as compared to other reports on SnO₂ NW gas sensors (Figure S6).²¹ However, in order to increase the amount of analytical information provided by the sensor, its operating parameters were modulated during the analyte exposure test. To elaborate, the operating parameters of heater temperature (T_{heater}) and gate bias (V_{gs}) were each varied according to their own continuously repeating pattern during the entire sensing experiment; see Fig. 2a. A single repetition of these patterns, which corresponded to a time period of 76.8 s, will be referred to as a parameter modulation cycle. During each of these modulation cycles, T_{heater} was varied between 194 °C and 373 °C at seven distinct temperature levels and

V_{gs} was varied between -5 V and 5 V in 2.5 V steps. These step changes occurred in a rapid fashion: T_{heater} was stepped every 6.4 s and V_{gs} was stepped every 0.8 s.

In order to monitor the state of the sensor during each of these discrete operating conditions, the sensor conductance was measured every 200 ms throughout the experiment. Moreover, measurements were synchronized such that acquisition consistently began 10 ms subsequent to changes in T_{heater} or V_{gs} . As has been observed previously, these measurements revealed that the MOX sensor conductance responded in a transient manner to step-shaped changes in T_{heater} and V_{gs} (Figure S7).^{38,39} In particular, initial changes in sensor conductance were observed to occur within the first measurement window following a perturbation of either T_{heater} or V_{gs} . This feature indicates that the operating state of the sensor was in fact rapidly affected by changes in the operating conditions and provides a basis for the rapid modulation approach that was employed in the experiment. An example of the raw output conductance signal that was recorded while operating the sensor using this approach is shown in Fig. 2a. Although the conductance behavior was complex, the sensor generally responded as expected with higher temperature and gate biases generally corresponding to a higher sensor conductance.

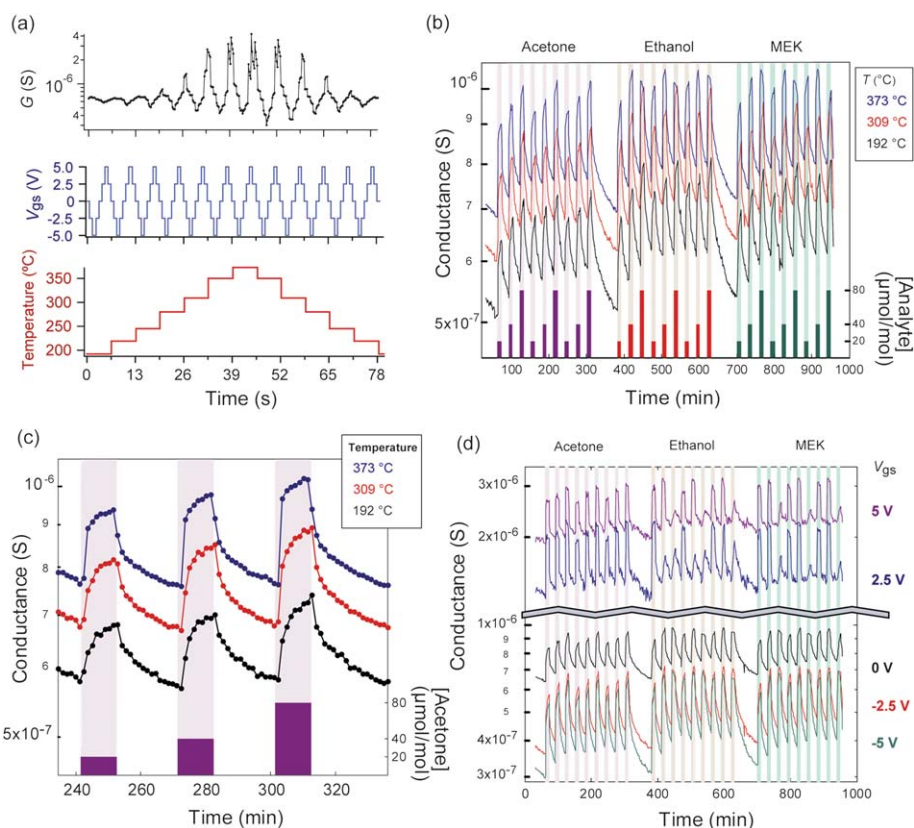


Fig. 2 Sensor Measurements from Validation Run. (a) Plot showing a single sensor measurement/modulation cycle. Lower, temperature cycling profile. Middle, gate voltage cycling profile. Upper, output sensor conductance measurements under dry air. Note that the plots display the start of a new cycle beginning at $t = 76.8$ s for clarity purposes. (b) Traces, left axis, sensor conductance measurements taken at 3 different temperatures during the validation run ($V_{gs} = 0$ V). Bars, right axis, analyte flow schedule for a single exposure run. (c) Zoomed in graph of part b, shows acetone exposures at three different concentrations. Each point in the graph corresponds to a single measurement sample extracted from a single measurement cycle. (d) Sensor conductance taken at 5 different V_{gs} conditions during the validation run ($T_{heater} = 373$ °C). Shading is used in b, c, and d to indicate regions of analyte exposure.

Using this rapid operating parameter modulation approach, the multi-analyte recognition capability of the sensor was tested using a 960 min long chemical vapor exposure sequence. The VOCs that served as analytes were acetone, ethanol, and methyl ethyl ketone (MEK). Analytes were exposed individually according to the exposure sequence shown in Fig. 2b. Three different analyte concentration levels were used (20 $\mu\text{mol/mol}$, 40 $\mu\text{mol/mol}$, and 80 $\mu\text{mol/mol}$) so as to increase the challenge of the recognition task. Three runs of this 960 min gas exposure sequence were carried out in a successive fashion during the length of the sensing experiment. The first run served to stabilize the sensor to the testing environment, the second run was used to collect measurement data for sensor training purposes (training phase), and the third run served as the VOC analyte recognition problem (validation phase).

3. Results and discussion

3.1 Sensor measurement signal extraction procedure

The analyte recognition capability of the modulated sensor was evaluated using the following analysis procedure. This procedure consisted of two separate stages: (1) signal extraction and pre-processing, and (2) pattern recognition analysis. A flow chart diagram that summarizes each of these stages is included in Figure S8.

First, in order to organize and simplify the complex sensor output for data analysis purposes, a set of simpler measurement signals were extracted from the raw sensor output. Specifically, each of the sensor measurements that was recorded during a modulation cycle was assigned to its own distinct signal, corresponding to a total of 384 signals (*i.e.*, 4 measurements per V_{gs} step, 8 V_{gs} steps per T_{heater} step, 12 T_{heater} steps per modulation cycle). For analytical purposes, each of these extracted signals will be understood to constitute a single dimension of a sensor output that encompasses a 384-dimensional feature space.

The rationale behind using this signal extraction scheme will now be presented. To this end, a plot of a selected set of extracted, uni-dimensional sensor output curves is shown in Fig. 2b. These curves comprise measurement signals corresponding to three separate T_{heater} values and an identical gate bias, $V_{\text{gs}} = 0$ V. A zoomed-in view of these sensor response curves for three acetone exposures is shown in Fig. 2c. Note that the generated curves are smooth and resemble the typical chemiresistive response of an unmodulated MOX sensor; *i.e.*, the sensor conductance rises during exposure to VOC analytes and recovers after the exposure ceases. A similar observation can be made for measurements conducted at different values of V_{gs} (Fig. 2d, $T_{\text{heater}} = 373$ °C). These plot characteristics suggest that the employed signal extraction scheme was effectively able to isolate the sensor's analyte response behavior from the ongoing changes in the sensor baseline conductance due to T_{heater} and V_{gs} modulations. A basis for this claim can be found by noting that the modulations of T_{heater} and V_{gs} were carried out in a consistent manner throughout the entire experiment. As a result, it is likely that the sensor resided in a relatively similar operating state during each of the consistently synchronized measurements that comprise these extracted signals. It can also be observed that each of the uni-dimensional curves shown in Fig. 2b,c,d are

visually distinct, thereby indicating that the sensor recorded non-redundant data due to its modulated mode of operation.

Next, pre-processing of these signals was carried out using the combined application of two techniques, range scaling and mean centering. These data pre-processing steps were carried out to rescale the response signals to compensate for the changes in baseline conductance due to the use of different temperatures and gate-bias conditions and to additionally compensate for long-term sensor drift (see Supporting Information†).^{35,40}

3.2 Pattern recognition analysis of the sensor response

In the next stage of the sensor data analysis, the identities of the exposed analytes were determined using a statistical training/recognition procedure. For analytical purposes, the procedure divided the 960 min long gas exposure run into hundreds of 76.8 s long subsections that each corresponded to individual sensor modulation cycles. Based on a pattern recognition analysis of the sensor conductance measurements, the statistical procedure attempted to identify the correct test gas (*i.e.*, acetone, ethanol, MEK, or dry air only) that was present during each of the sensor modulation cycles. In particular, the temperature- and gate-dependent variations in the sensor's chemiresistive response that were noted in Fig. 2 were utilized as a "fingerprint" for analyte identification purposes in the pattern recognition procedure.

To elaborate, this pattern recognition procedure used the following statistical, multivariate dimensional reduction and classification methods. First, linear discriminant analysis (LDA) was performed on the multi-dimensional sensor output that was extracted from training phase measurements. LDA was used to find an optimal linear transform that mapped the measurements to a lower-dimensionality space while preserving analyte-specific data features.⁴¹ This LDA-derived data transform was then applied to measurement data collected during the validation phase for similar dimensionality reduction purposes. Finally, classification of the dimensionally reduced validation phase measurements was carried out using a k -nearest neighbor classification method to obtain final test gas identification results. The resulting classified form of the measurements is presented for visual purposes using 3-D scatter plots, *e.g.* Fig. 3a,b. See Supporting Information† for additional details.

Although LDA is a capable pattern recognition procedure, LDA itself does not have the ability to evaluate the relative usefulness of different input measurement signals, *i.e.*, dimensions, in training/recognition tasks. Due to this deficiency, the effectiveness of LDA-based training/recognition procedures can be negatively affected by the presence of input data that are not relevant to the classification task.³⁵ To address this issue, a comparative analysis was carried out to investigate the usefulness of each of the examined temperatures and gate biases towards obtaining the highest VOC recognition accuracy. To this end, the LDA-based analyte training/recognition procedure was carried out multiple times using different sets of signals that were obtained from the sensor output using the previously described signal extraction scheme. These extracted signals each consisted of measurements conducted at certain, unique operating conditions (*i.e.*, V_{gs} and T_{heater} values), which in turn are regarded as corresponding to different sensor operational states. The average VOC recognition accuracies that were obtained from each of

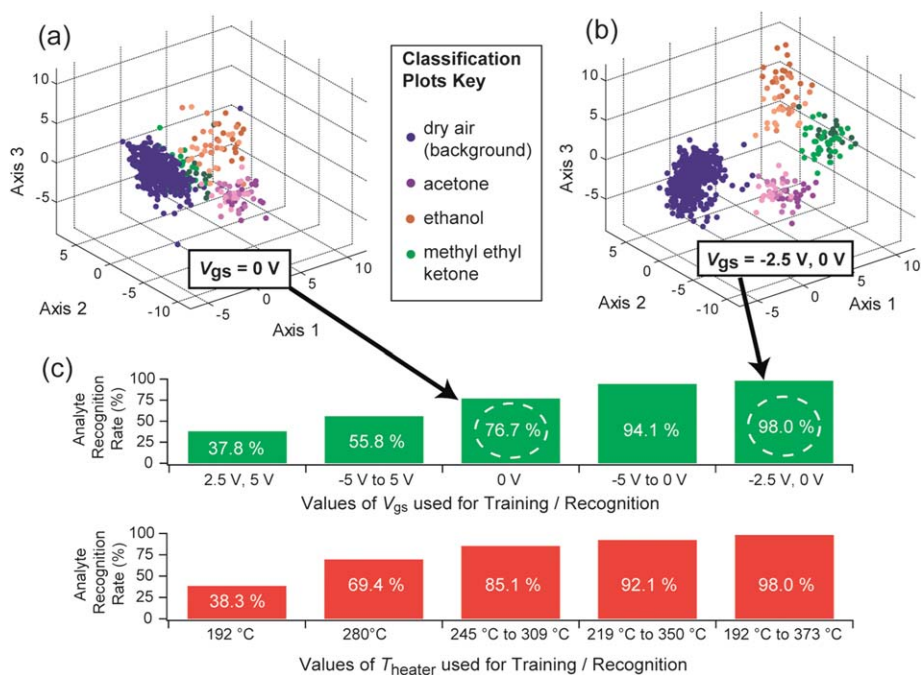


Fig. 3 Analysis of Analyte Recognition Results. (a) 3-D, LDA-derived scatter plot generated for recognition purposes during the validation run using sensor data recorded for $T_{\text{heater}} = 194\text{ }^{\circ}\text{C}$ to $373\text{ }^{\circ}\text{C}$, $V_{\text{gs}} = 0\text{ V}$. The color of the scatter points denotes the actual exposed analyte so as to provide a visual indication of the discrimination ability of the sensor. The lighter to darker shades of color used for point coloring indicate different analyte concentrations ($20\text{ }\mu\text{mol/mol}$, $40\text{ }\mu\text{mol/mol}$, $80\text{ }\mu\text{mol/mol}$). Darker shades correspond to higher analyte concentrations. (b) LDA-derived plot generated using sensor data recorded for operating parameter values $T_{\text{heater}} = 194\text{ }^{\circ}\text{C}$ to $373\text{ }^{\circ}\text{C}$, $V_{\text{gs}} = -2.5\text{ V}$ and 0 V . (c) Plots displaying the effect of the use of modulated sensor conditions on the average analyte recognition rate. Upper, sensor data recorded when $T_{\text{heater}} = 194\text{ }^{\circ}\text{C}$ to $373\text{ }^{\circ}\text{C}$ and V_{gs} was varied among different conditions. Critically, utilizing sensor data recorded when $V_{\text{gs}} = -2.5\text{ V}$ and 0 V produces superior recognition results than utilization of sensor data recorded only at a single bias condition of $V_{\text{gs}} = 0\text{ V}$. Lower, plot showing effects of various T_{heater} measurement conditions on recognition accuracy when $V_{\text{gs}} = -2.5\text{ V}$, 0 V .

these analysis runs were then compared against each other. See Figure S8 for an overview of this comparative analysis.

3.3 Analyte recognition performance analysis

To begin this analysis of the analyte recognition capability of the modulated sensor, the effect of gate-bias conditions on the sensor's recognition accuracy will be examined. First, classification results generated from the statistical analysis of measurements conducted at two different sets of V_{gs} conditions will be compared. A scatter plot of the classification result produced from sensor measurements carried out only when the gate was in a grounded state and inclusive of all temperature conditions is shown in Fig. 3a. Notably, an improvement in analyte cluster separability was achieved after inclusion of a second gate bias ($V_{\text{gs}} = -2.5\text{ V}$) in the analysis, as shown in Fig. 3b. Quantifiably, the separation distance between analyte clusters in these graphs, as described using their average Mahalanobis distance,¹³ increased from 4.74 to 7.81 by incorporation of $V_{\text{gs}} = -2.5\text{ V}$ in addition to $V_{\text{gs}} = 0\text{ V}$. In multivariate analysis, analyte cluster separability is considered a direct measure of the discrimination capability of a sensor.³⁶ Moreover, the recognition success rate also showed an improvement; the obtained recognition accuracy increased from 76.7% to 98.0% for these two cases. Overall, this result demonstrates that the combined use of rapid gate and temperature modulation can be utilized to improve the selectivity

of a MOX NW sensor. See Tables S1 to S3 for detailed information on the recognition performance of the sensor.

Importantly, however, further runs of the recognition procedure on additional sets of gate-bias conditions revealed that poor recognition results were associated with certain gate biases, as shown in Fig. 3c. For instance, a recognition accuracy of just 37.8% was obtained through the use of measurements conducted at positive gate biases ($V_{\text{gs}} = 2.5\text{ V}$ and 5 V). This result indicates that the extracted signals corresponding to these positive bias conditions possessed features that were less relevant for achieving discrimination between the examined VOC analytes. Consequently, optimization of the sensor modulation and measurement procedure may provide a route for the future improvement of the recognition accuracy of this type of gas sensor.

A similar analysis examining the effect of temperature on recognition accuracy is included in Fig. 3c. Recognition accuracy is found to increase with the inclusion of additional temperatures in the training/recognition procedure, a result that has been extensively described in previous studies of MOX sensors.³⁵ Additionally, inclusion of all four of the measurements conducted during each 0.8 s long V_{gs} step enhanced the VOC recognition accuracy of the sensor and all were included in the previous comparative analysis (see Figure S9). This positive benefit suggests that these successive measurements recorded gate-induced sensor conductance transients that contained

additional information that assisted the discrimination task.³⁸ Overall, it is important to note that this comparative analysis of the effect of various gate biases and temperatures was performed in a single experiment and on a single sensor device thereby avoiding the separate problems of SnO₂ nanowire sensor aging, *i.e.*, drift over the time range of days,⁴² and nanowire device-to-device variations.⁴³

3.4 Optimized analyte recognition performance

As described in the previous section, the sensor operating conditions that optimized the recognition accuracy of the modulated sensor in this specific gas recognition task were found to comprise $V_{gs} = -2.5$ V, 0 V and $T_{heater} = 192$ °C to 373 °C. A plot that displays the complete recognition results that were obtained using sensor measurements associated with these operating conditions is shown in Fig. 4. Overall, just 5 misclassifications occurred during the entire 960 min long exposure sequence, where the 960 min long exposure test was divided into 600 discrete time segments, *i.e.* sensor modulation cycles. This corresponds to an overall recognition rate (including background, dry air only exposures) of 99.2% and a 98.0% analyte recognition rate that excludes background only exposures. More detailed recognition results are given in the confusion matrix in Table S2.

Examination of the raw sensor conductance signal at the time periods associated with these misclassifications revealed that sudden spike-shaped disturbances in the signal had occurred at these times. These disturbances are most likely the result of environmental electromagnetic and vibrational disturbances, and could be avoided in future studies through the use of improved environmental shielding as well as an additional

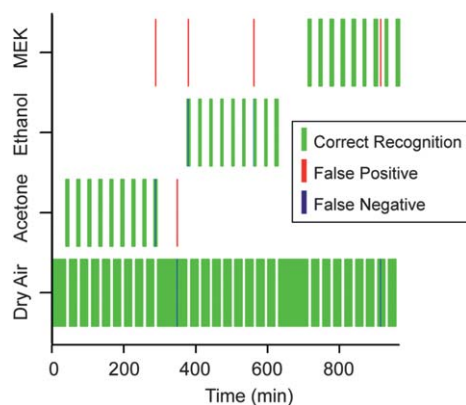


Fig. 4 Optimized Analyte Recognition Results. Analyte recognition results obtained by using sensor measurements conducted at $V_{gs} = -2.5$ V, 0 V and $T_{heater} = 192$ °C to 373 °C. Plot displays analyte determinations made for exposures that occurred during the validation phase of the sensor test. The recognition results comprise 600 discrete analyte determinations, *i.e.*, each determination was made based off of sensor measurements taken during separate sensor modulation cycles that occurred during the validation phase. Coloring (see key) is used to indicate whether the analyte determination was either correct, a false positive, or a false negative. Analyte (acetone, ethanol, and MEK) concentrations range from 20 $\mu\text{mol/mol}$ to 80 $\mu\text{mol/mol}$ in a dry air background. Analyte determinations were not attempted for modulation cycles that overlapped an analyte change event.

amount of sensing nanowires to improve the signal-to-noise ratio of the device.

On the whole, these optimized recognition results attest to the capability of this modulated sensor to successfully recognize multiple VOC analytes. Although this result is promising, additional studies are required to determine the ability of this sensor to recognize individual analytes in mixtures, analytes in broader concentration ranges, and analyte concentration levels.

3.5 Gate modulation and its effect on sensor selectivity

Although the use of both gate and temperature modulation were shown to enhance the selectivity of the SnO₂ nanowire sensor, the benefits provided by the use of temperature modulation have been explored extensively in other studies on MOX sensors;^{24,44} as such, the effect of gate modulation will be examined here exclusively. The physical basis for the selectivity improvement that was gained through the use of gate modulation can be understood by examining the chemical processes that take place at the surface of a SnO₂ gas sensor. It is well-known that under the testing conditions explored in this work (temperature ≈ 200 °C to 400 °C, dry air background, and VOCs at concentrations from 20 $\mu\text{mol/mol}$ to 80 $\mu\text{mol/mol}$) that oxygen is the predominant chemisorbed species on the surface of tin oxide.⁴⁵ Chemisorbed oxygen species, in the form of dissociated O⁻ ions, act to withdraw electrons from the SnO₂ resulting in the formation of a depletion layer, estimated to ≈ 10 nm to ≈ 15 nm in depth,^{46,47} and upwards band bending at the semiconductor surface.⁴⁸ Exposure of SnO₂ to reducing gas analytes, such as VOCs, causes a reduction in the depth of this depletion region and a corresponding increase in the conductance of the sensor. This chemiresistive response is a result of surface redox processes that act to catalytically oxidize reducing gas species and simultaneously to reduce the amount of surface oxygen species.⁴⁹ These redox processes proceed according to the multi-step Mars-van Krevelen mechanism that involves: (a) chemisorption of the reactant oxygen and analyte species, and subsequently (b) catalytic oxidation of the reducing gas analyte.^{50,51}

Based on this description of the chemical reactions that occur at the sensor surface, the selectivity improvement provided by the use of gate modulation will now be examined. For this discussion, the electronic theory of chemisorption and catalysis on semiconductors, initially proposed by Hauffe, will be employed.⁵² This theory describes chemisorption and catalysis on an electronic basis by treating the charge transfer that occurs between the semiconductor surface and chemisorbed species during these processes as a source of surface band bending. As a consequence of this theory, these chemical processes are believed to be regulated according to the relative alignment of the semiconductor's Fermi level (E_f) with the redox level of reacting adsorbed species (E_{redox}).⁵³ In order to examine the practical effect of this theory, the energy band diagram that describes the charge transfer process that occurs during the chemisorption of a reducing gas is schematically outlined in Fig. 5a. Practically, this figure indicates that the rate of electron transfer that is associated with chemisorption of the reducing gas species is dependent on the distance that E_{redox} lies above E_f .⁵⁴

The use of gate modulation, however, can affect the lineup of these energy levels and thus act to modulate sensing behavior. To

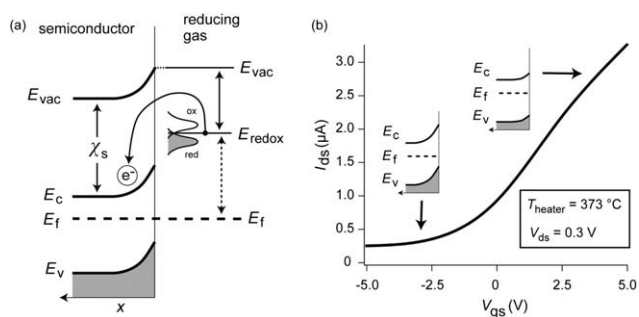


Fig. 5 Effect of Gating on the SnO₂ Nanowire Sensor. (a) Band diagram schematic that qualitatively describes the chemisorption reaction of reducing gases onto the surface of a SnO₂ semiconductor. The reducing gas molecule is represented as a redox couple.⁵⁴ Note that this schematic represents the energy level arrangement immediately before chemisorption and electron transfer occurs. As shown in this figure, chemisorption and electron transfer to the semiconductor is energetically favored to occur and proceeds at a rate that is proportional to the distance that E_{redox} lies above E_f . The shaded region represents allowed energy states that are occupied by electrons at this time. Definition of terms: χ_s - electron affinity of the semiconductor, E_c - semiconductor conduction band, E_v - semiconductor valence band, E_{vac} - vacuum level, x - distance below the semiconductor surface. The upwards surface band bending that is shown in this figure is used to indicate the presence of adsorbed oxygen.^{45,48} The parabolic-shaped density of states of the oxidized (R⁺) and reduced (R) forms of the reducing gas analytes are shown. (b) Sweep of I_{ds} versus V_{gs} taken in a dry air environment, $T_{\text{heater}} = 373$ °C, and $V_{\text{ds}} = 0.3$ V. Upper left, a qualitative schematic illustrating the hypothesized change in band bending that occurs at the surfaces of the semiconductor. Upon increases in V_{gs} , the energy bands at the surfaces of the semiconductor are expected to move in a downwards direction relative to E_f .

elaborate; first, alteration of the gate bias of a nanowire FET induces a modulation in the nanowire's surface band bending. Due to this change in band bending, *i.e.*, shifting of the nanowire's conduction and valence bands, the position of E_f at the surface can be expected to change relative to E_{redox} . Using the electronic theory of chemisorption, this shift in the relative position of E_f is predicted to modify the rates of chemisorption and catalytic reaction in a manner described by Fermi occupancy statistics.⁵⁵ Moreover, due to the fact that the position of the redox level of surface-bound analyte species (E_{redox}) is analyte-specific, it becomes evident that the described gate-dependent sensing effect is itself expected to be analyte-specific, as previous studies have suggested.^{25,56} Overall, the use of a gate bias to shift the position of E_f during sensor operation can be expected to generate analyte-specific sensor behavior and provides a basis for the noted improvement in analyte recognition with the use of gate modulation.

Although a qualitative description of the use of the gate to improve selectivity has been presented, a more thorough discussion that explains the finding that certain gate biases, *i.e.*, $V_{\text{gs}} = 0$ V and -2.5 V, were found to be the most useful for achieving recognition of the selected VOC analytes is beyond the scope of this work. In particular, the presence of complicating factors makes attempts to further analyze the experimental results prohibitively complex. Two of these factors include: (1) the use of rapid gate modulation as opposed to static gate

conditions, and (2) the possible variation in chemisorption and catalysis with respect to different nanowire surface facets.^{57,58}

In order to verify the claim that alteration of the V_{gs} bias modulated the band bending of the semiconductor, electrical characterization of the nanowire field-effect transistor (NW-FET) sensor was carried out. Testing revealed that the sensor's back-gate operated in a manner identical to previous reports on NW-FETs.⁵⁹ As shown in Fig. 5b, the sensor showed an expected n-type response with the current through the device changing from 0.25 μA to 3.27 μA during a V_{gs} sweep from -5 V to 5 V. Moreover, these results indicate that the NW-FET was a depletion-mode device, as its threshold voltage (V_{th}) was less than 0 V. Testing conditions for the gate sweep were $T_{\text{heater}} = 373$ °C, $V_{\text{ds}} = 0.3$ V, and a dry air background. Contact-related Schottky effects on the I - V behavior of the sensor were ruled out through additional testing (Figure S10). Thus, the observed current modulation can confidently be concluded to have resulted from gate-induced changes in the band bending of the semiconductor, *i.e.*, the depletion/accumulation of carriers in the bulk of the nanowire.

In order to verify that the back-gate was able to modulate the band-bending at all exposed surfaces of the sensing SnO₂ nanowires and not just the surfaces closest to the back-gate, a 2-D electrostatic simulation was performed (See Figure S11 and associated discussion). To this end, the simulation examined the extent that the electric-field that emanated from the back-gate was able to couple with the surfaces of the nanowires employed by the sensor and was carried out in a similar fashion to previous NW-FET simulation work.⁶⁰ The results of this simulation, which considered the interaction of a single nanowire (50 nm diameter) with the back-gate ($V_{\text{gs}} = 1$ V), are shown in Fig. 6. From this cross-sectional profile of the electric-field surrounding a nanowire, a significant amount of electric-field coupling can be observed between the back-gate and the three exposed nanowire surfaces, *i.e.*, the surfaces that are not in contact with the SiN_x insulator. Due to their direct contact with ambient gases, these three surfaces can be assumed to dominate the sensing response of a SnO₂ nanowire. The noticeable amount of electric-field coupling at these interfaces indicates that a considerable amount of mutual capacitance was present between these surfaces and the back-gate. By analyzing the simulated electric-field profile, the capacitance of these exposed surfaces was found to account for a substantial fraction (24.8%) of the total amount of gate-NW capacitance. See Supporting Information† for additional details regarding this simulation and analysis.

Based on this result, adjustments of the gate bias can be expected to induce a significant change in the band bending at the semiconductor surface, *i.e.*, the relative position of E_f , and in turn to affect the charge transfer processes that are known to occur between adsorbates and the NW bulk. This effect illustrates the benefit of employing nanowires in back-gate modulated sensors. In comparison, the use of thin-film sensing materials in this back-gate sensor design would not allow for substantial gate coupling to exposed sensing surfaces. Moreover, the magnitude of gate coupling to these exposed SnO₂ surfaces can be increased in future nanowire sensor designs through the use of either thinner gate dielectrics or narrower diameter nanowires.

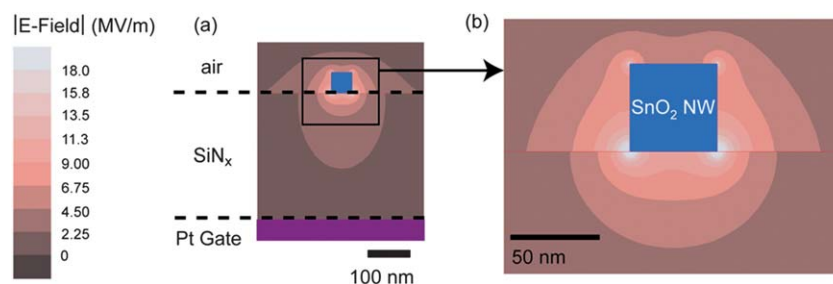


Fig. 6 2-D Electrostatic Simulation of the Gate-Induced Electric-Field. Specifically, this simulation considered the electrostatic interaction of the back-gate with a single nanowire employed by the sensor. (a) Cross-sectional view of the simulated electric-field profile surrounding a single nanowire in the sensor active area under a bias of $V_{gs} = 1$ V. The nanowire is grounded. (b) Zoomed-in view of the electric-field profile around the nanowire. A substantial amount of electric-field coupling is evident between the back-gate and the exposed nanowire surfaces which are furthest away from the back-gate.

4. Conclusion

In summary, an approach that utilized the combined rapid modulation of both the temperature and gate-bias conditions of a nanowire FET sensor was found to greatly enhance its VOC recognition capabilities. Specifically, through the use of optimized multivariate statistical methods, an average recognition rate of 98.0% was obtained for the sensor in a VOC analyte exposure test. In particular, it was determined using a comparative analysis that optimal recognition rates could only be achieved through the modulation of both gate bias and temperature as compared to either parameter alone. For instance, a significantly lower average recognition rate of 76.7% was obtained using measurements that were taken exclusively when the gate was in a grounded state. Altogether, these results show that the combined use of temperature and gate modulation provided for an increase in the analyte discrimination capability of the sensor.

This dual modulation approach was enabled by the use of a microhotplate platform featuring an integrated back-gate electrode. The sensor platform, constructed using standard microfabrication techniques, possessed low power requirements and a small spatial footprint, making it well-suited for portable and networked sensing applications. Additionally, single-crystalline SnO_2 nanowires were utilized as the transducer material. Their high surface-area-to-volume morphology and large carrier mobilities allowed for the high degree of gate control that was required by this study. Although analyte selectivity results were favorable with the utilized SnO_2 nanowires, the examined temperature/gate modulation approach to nanowire sensing is applicable to any gas-sensitive semiconducting nanowire material. Overall, the desirable combination of a miniature footprint and a high VOC analyte selectivity that was demonstrated in the examined nanowire sensor indicates that the potential exists for the practical use of nanowire sensors in multi-gas recognition applications.

Acknowledgements

E.N.D. acknowledges support provided through the NIST-National Research Council (NRC) Postdoctoral Associateship Program and valuable assistance from Phil Rogers, Chip Montgomery, Michael Carrier, Steve Semancik, and Sergiy Krylyuk (NIST).

References

- 1 Y. Cui, Q. Wei, H. Park and C. M. Lieber, *Science*, 2001, **293**, 1289–1292.
- 2 M. Li, R. B. Bhiladvala, T. J. Morrow, J. A. Siooss, K.-K. Lew, J. M. Redwing, C. D. Keating and T. S. Mayer, *Nat. Nanotechnol.*, 2008, **3**, 88–92.
- 3 C. Soci, A. Zhang, B. Xiang, S. A. Dayeh, D. P. R. Aplin, J. Park, X. Y. Bao, Y. H. Lo and D. Wang, *Nano Lett.*, 2007, **7**, 1003–1009.
- 4 E. Comini, G. Faglia, G. Sberveglieri, Z. Pan and Z. L. Wang, *Appl. Phys. Lett.*, 2002, **81**, 1869–1871.
- 5 Q. Wan, Q. H. Li, Y. J. Chen, T. H. Wang, X. L. He, J. P. Li and C. L. Lin, *Appl. Phys. Lett.*, 2004, **84**, 3654–3656.
- 6 D. Zhang, Z. Liu, C. Li, T. Tang, X. Liu, S. Han, B. Lei and C. Zhou, *Nano Lett.*, 2004, **4**, 1919–1924.
- 7 A. Ponzoni, E. Comini, G. Sberveglieri, J. Zhou, S. Z. Deng, N. S. Xu, Y. Ding and Z. L. Wang, *Appl. Phys. Lett.*, 2006, **88**, 203101–203103.
- 8 A. Kolmakov and M. Moskovits, *Annu. Rev. Mater. Res.*, 2004, **34**, 151–180.
- 9 D. C. Meier, B. Raman and S. Semancik, *Annu. Rev. Anal. Chem.*, 2009, **2**, 463–484.
- 10 B. Buszewski, M. Keszy, T. Ligor and A. Amann, *Biomed. Chromatogr.*, 2007, **21**, 553–566.
- 11 K. D. Benkstein, B. Raman, C. B. Montgomery, C. J. Martinez and S. Semancik, *IEEE Sens. J.*, 2010, **10**, 137–144.
- 12 J. M. Baik, M. Zielke, M. H. Kim, K. L. Turner, A. M. Wodtke and M. Moskovits, *ACS Nano*, 2010, **4**, 3117–3122.
- 13 V. V. Sysoev, E. Strelcov, M. Sommer, M. Bruns, I. Kiselev, W. Habicht, S. Kar, L. Gregoratti, M. Kiskinova and A. Kolmakov, *ACS Nano*, 2010, **4**, 4487–4494.
- 14 V. V. Sysoev, J. Goschnick, T. Schneider, E. Strelcov and A. Kolmakov, *Nano Lett.*, 2007, **7**, 3182–3188.
- 15 P.-C. Chen, F. N. Ishikawa, H.-K. Chang, K. Ryu and C. Zhou, *Nanotechnology*, 2009, **20**, 125503.
- 16 K. Scholten, F. I. Bohrer, E. Dattoli, W. Lu and E. T. Zellers, *Nanotechnology*, 2011, **22**, 125501.
- 17 F. Rock, N. Barsan and U. Weimar, *Chem. Rev.*, 2008, **108**, 705–725.
- 18 D. M. Wilson, S. Hoyt, J. Janata, K. Booksh and L. Obando, *IEEE Sens. J.*, 2001, **1**, 256–274.
- 19 W. Göpel, *Sens. Actuators, B*, 1998, **52**, 125–142.
- 20 A. Heilig, N. Barsan, U. Weimar, M. Schweizer-Berberich, J. W. Gardner and W. Göpel, *Sens. Actuators, B*, 1997, **43**, 45–51.
- 21 D. C. Meier, S. Semancik, B. Button, E. Strelcov and A. Kolmakov, *Appl. Phys. Lett.*, 2007, **91**, 063118–063113.
- 22 Z. Fan, D. Wang, P.-C. Chang, W.-Y. Tseng and J. G. Lu, *Appl. Phys. Lett.*, 2004, **85**, 5923–5925.
- 23 A. P. Lee and B. J. Reedy, *Sens. Actuators, B*, 1999, **60**, 35–42.
- 24 S. Semancik, R. E. Cavicchi, M. C. Wheeler, J. E. Tiffany, G. E. Poirier, R. M. Walton, J. S. Suehle, B. Panchapakesan and D. L. DeVoe, *Sens. Actuators, B*, 2001, **77**, 579–591.
- 25 Y. Zhang, A. Kolmakov, Y. Lilach and M. Moskovits, *J. Phys. Chem. B*, 2005, **109**, 1923–1929.
- 26 N. Barsan, D. Koziej and U. Weimar, *Sens. Actuators, B*, 2007, **121**, 18–35.

- 27 Q. Wan, J. Huang, Z. Xie, T. Wang, E. N. Dattoli and W. Lu, *Appl. Phys. Lett.*, 2008, **92**, 102101–102103.
- 28 S. Mubeen and M. Moskovits, *Adv. Mater.*, 2011, **23**, 2306–2312.
- 29 F. Hernandez-Ramirez, J. D. Prades, R. Jimenez-Diaz, T. Fischer, A. Romano-Rodriguez, S. Mathur and J. R. Morante, *Phys. Chem. Chem. Phys.*, 2009, **11**, 7105–7110.
- 30 E. N. Dattoli, Q. Wan, W. Guo, Y. Chen, X. Pan and W. Lu, *Nano Lett.*, 2007, **7**, 2463–2469.
- 31 Q. Wan, E. N. Dattoli and W. Lu, *Appl. Phys. Lett.*, 2007, **90**, 222107–222103.
- 32 Z. Fan, J. C. Ho, Z. A. Jacobson, R. Yerushalmi, R. L. Alley, H. Razavi and A. Javey, *Nano Lett.*, 2008, **8**, 20–25.
- 33 Z. Fan, J. C. Ho, Z. A. Jacobson, H. Razavi and A. Javey, *Proc. Natl. Acad. Sci. U. S. A.*, 2008, **105**, 11066–11070.
- 34 J. Courbat, D. Briand and N. F. de Rooij, *Sens. Actuators, A*, 2008, **142**, 284–291.
- 35 A. Hierlemann and R. Gutierrez-Osuna, *Chem. Rev.*, 2008, **108**, 563–613.
- 36 B. Raman, D. C. Meier, J. K. Evju and S. Semancik, *Sens. Actuators, B*, 2009, **137**, 617–629.
- 37 M. Afridi, C. B. Montgomery, E. Cooper-Balis, S. Semancik, K. G. Kreider and J. Geist, *IEEE Electron Device Lett.*, 2009, **30**, 928–930.
- 38 R. Gutierrez-Osuna, A. Gutierrez-Galvez and N. Powar, *Sens. Actuators, B*, 2003, **93**, 57–66.
- 39 J. Maeng, W. Park, M. Choe, G. Jo, Y. H. Kahng and T. Lee, *Appl. Phys. Lett.*, 2009, **95**, 123101.
- 40 F. Hernandez-Ramirez, J. D. Prades, A. Tarancon, S. Barth, O. Casals, R. Jimenez-Diaz, E. Pellicer, J. Rodriguez, J. R. Morante, M. A. Juli, S. Mathur and A. Romano-Rodriguez, *Adv. Funct. Mater.*, 2008, **18**, 2990–2994.
- 41 P. C. Jurs, G. A. Bakken and H. E. McClelland, *Chem. Rev.*, 2000, **100**, 2649–2678.
- 42 V. V. Sysoev, T. Schneider, J. Goschnick, I. Kiselev, W. Habicht, H. Hahn, E. Strelcov and A. Kolmakov, *Sens. Actuators, B*, 2009, **139**, 699–703.
- 43 F. N. Ishikawa, M. Curreli, H.-K. Chang, P.-C. Chen, R. Zhang, R. J. Cote, M. E. Thompson and C. Zhou, *ACS Nano*, 2009, **3**, 3969–3976.
- 44 G. Korotcenkov, *Mater. Sci. Eng., B*, 2007, **139**, 1–23.
- 45 M. E. Franke, T. J. Koplín and U. Simon, *Small*, 2006, **2**, 36–50.
- 46 D. Serghei, *et al.*, *Nanotechnology*, 2007, **18**, 055707.
- 47 E. Comini, V. Guidi, C. Malagù, G. Martinelli, Z. Pan, G. Sberveglieri and Z. L. Wang, *J. Phys. Chem. B*, 2004, **108**, 1882–1887.
- 48 N. Barsan and U. Weimar, *J. Electroceram.*, 2001, **7**, 143–167.
- 49 S. H. Hahn, N. Bârsan, U. Weimar, S. G. Ejakov, J. H. Visser and R. E. Soltis, *Thin Solid Films*, 2003, **436**, 17–24.
- 50 J. Haber and M. Witko, *J. Catal.*, 2003, **216**, 416–424.
- 51 J. J. Spivey, *Ind. Eng. Chem. Res.*, 1987, **26**, 2165–2180.
- 52 C. O. Park and S. A. Akbar, *J. Mater. Sci.*, 2003, **38**, 4611–4637.
- 53 H. Geistlinger, *Sens. Actuators, B*, 1993, **17**, 47–60.
- 54 M. Batzill and U. Diebold, *Prog. Surf. Sci.*, 2005, **79**, 47–154.
- 55 S. M. Sze and K. K. Ng, *Physics of Semiconductor Devices*, Wiley-Interscience, 2007.
- 56 Y. Zhang, A. Kolmakov, S. Chretien, H. Metiu and M. Moskovits, *Nano Lett.*, 2004, **4**, 403–407.
- 57 Z. R. Dai, J. L. Gole, J. D. Stout and Z. L. Wang, *J. Phys. Chem. B*, 2002, **106**, 1274–1279.
- 58 D. H. Kim, W.-S. Kim, S. B. Lee and S.-H. Hong, *Sens. Actuators, B*, 2010, **147**, 653–659.
- 59 W. Lu and C. M. Lieber, *J. Phys. D: Appl. Phys.*, 2006, **39**, R387.
- 60 D. R. Khanal and J. Wu, *Nano Lett.*, 2007, **7**, 2778–2783.